Empirical Evidence of Frequency-Dependent Directivity Effects from Small-to-Moderate Normal Fault Earthquakes in Central Italy

Leonardo Colavitti[1], Giovanni Lanzano[1], Sara Sgobba[1], Francesca Pacor[1], Frantisek Gallovič[2]

[1] National Institute of Geophysics and Volcanology, Section of Seismology applied to Engineering, Milano, Italy

[2] Charles University, Faculty of Mathematics and Physics, Department of Geophysics, Prague, Czech Republic

Corresponding author: Leonardo Colavitti (leonardo.colavitti@ingv.it)

Key Points:

- Statistical procedure to detect directivity effects in small-to-moderate earthquakes analyzing the aleatory residuals of the ground motion
- The directive events are the 36% of the dataset and the distribution of rupture direction is aligned with the strikes of the faults system
- The observed directivity is a frequency-dependent band-limited phenomenon, which can occur up to 5 times the value of corner frequency

Abstract. Rupture directivity and its potential frequency dependence is an open issue within the seismological community, especially for small-to-moderate events. Here we provide a statistical overview based on empirical evidence of seismological observations, thanks to the large amount of high-quality seismic recordings (more than 30'000 waveforms) from Central Italy, which represents an excellent and almost unique natural laboratory of normal faulting earthquakes in the magnitude range of 3.4 and 6.5 within the time frame 2008-2018. In order to detect an anisotropic distribution of ground motion amplitudes due to the rupture directivity, we fit the smoothed Fourier Amplitude Spectra (FAS) cleared of source-, site- and path- effects. According to our criteria, about 36% of the analyzed events (162 out of 456) are directive and the distribution of rupture direction is aligned with the strikes of the major faults of the Central Apennines. We find that the directivity is strongest, up to approximately 5 times the event's corner frequencies. The results of this research provide useful insights to parameterize directivity as a frequency-dependent band-limited phenomenon, to be explicitly implemented in future ground motion modeling and scenario predictions.

Plain Language Summary. In seismology, directivity is one of the source phenomena that causes large spatial variability of earthquake ground motions and is related to the features of the rupture propagation along the fault. The importance of this effect is very well known for large-magnitude events (M > 6), while it is still an open issue for small-to-moderate events. The aim of this paper is to recognize directive events and quantify their strength in Central Italy, using a large dataset of earthquakes in the magnitude range 3.4-6.5 that occurred between 2008 and 2018. We find that about 36% of the analyzed events are directive, caused by rupture propagations oriented along the NW-SE alignment of the Central Apennines fault systems. Furthermore, we find that directivity is a band-limited phenomenon and that as the directivity gets stronger, the frequency band becomes wider. Our contribution provides a useful insight with the possibility to improve the parametrization of directivity within the empirical seismic hazard assessment.

1 Introduction

Directivity effect of an earthquake is the focusing of the radiated seismic wave energy due to the rupture propagation along the fault (Ben-Menahem, 1961; Joyner, 1991; Anderson, 2007; Boatwright, 2007). Earthquake directivity represents the analogue of the Doppler effect for sound and light waves (Douglas et al., 1988; Pacor et al., 2016a), which shifts the frequency of a moving oscillator to higher frequency when the oscillator moves toward an observer, and lower frequency when it moves away.

This phenomenon, which represents one of the key factors in featuring the spatial distribution of the seismic shaking, produces azimuthal and spectral variations in the ground motion, that can be used to infer information on both the orientation of the fault plane and on the modes of rupture propagation (Abercrombie et al., 2017). Furthermore, the quantification of the directivity-induced amplifications has important consequences in seismic hazard assessment, in terms of ground-motion amplitude and associated variability (Spagnuolo et al., 2012; Chioccarelli and Iervolino, 2014). Although the importance of directivity is widely recognized for both seismological studies on earthquake sources and engineering applications, a clear picture of how strongly and how often it occurs is not yet available.

In the 90s, the directivity phenomenon was initially observed and modelled for large events, such as the two recordings of the 1992 Mw 7.3 Landers earthquake at Lucerne and Joshua Tree stations (Velasco et al., 1994; Bernard et al., 1996; Pacor et al., 2005) or the 1994 Mw 6.7 Northridge earthquake (Somerville et al., 1996), since earthquake directivity was combined with the effects of the finite size of the fault. Over the years, with the development of the broad-band seismic networks, the data quantity and quality have improved considerably. For this reason, nowadays we are able to observe directivity even for moderate-sized (McGuire, 2004; Boatwright, 2007; Seekins and Boatwright, 2010; Courboulex et al., 2013; Calderoni et al., 2015; Convertito et al., 2016; Pacor et al., 2016a) and small earthquakes (Yamada et al., 2005; Tomic et al., 2009; Chen et al., 2010). Directivity in small earthquakes is not a sporadic phenomenon, and recent studies of large datasets in California (Ross et al., 2020) and Japan (Yoshida, 2019) have shown that asymmetric ruptures (unilateral) seem predominant with respect to symmetric ones (bilateral), occurring in more than 60% of the cases analyzed. Much more debated is the question of a prevailing direction of rupture propagation in a given region or during a seismic sequence. On this aspect, the results are controversial, as are the physical causes that might determine a preferred

direction. For instance, for the case of the 2012 Emilia seismic sequence in Italy, Convertito et al. (2013) observed that a variation of permeability might encourage the fracture in a preferred direction as a consequence of a local increase of the pore pressure and fluid flow rates: in this context, the source directivity can also enhance changes in permeability (López-Comino et al., 2021).

The effects of directivity on ground motion are magnitude and frequency dependent (Bernard and Herrero, 1994). At low frequencies and for moderate-to-strong events, directivity can be responsible for coherent, potentially very destructive pulses with large amplitudes, while at high frequencies and for small-to-moderate events, the most evident effect is given by the shift of the corner frequencies that can result in high-frequency energy arrivals in short time intervals (Anderson, 2007). Modeling of the 2014 Mw 6 Napa earthquake by Gallovič (2016) suggested a preference of model with weak or no directivity effect at high frequencies to correctly explain the azimuthal variations of the strong ground motions. Based on empirical observations from seismic recordings, Pacor et al. (2016a) showed that high-frequency directivity can weaken due to source complexity even for small events.

In the context of the ground motion models (GMMs), the directivity effects in seismic records are inferred by analyzing the frequency and azimuthal dependence of the residual terms corrected for systematic contributions related to the source and the sites (e.g. Ameri et al., 2009; Ren et al., 2017) and, in a fully non-ergodic approach, also to the path (Sgobba et al., 2021). Recently, this approach was adopted to recognize directivity effects during some events of the 2016-2017 Central Italy seismic sequence (Calderoni et al., 2015; Calderoni et al., 2017; Ren et al., 2017; Luzi et al., 2017), revealing significant rupture-propagation complexity, both for small and moderate earthquakes.

In light of the above, it is clear that the literature studies on directivity modeling are mainly carried out with the aim of interpreting the spatial patterns of specific recorded seismic sequences or in order to find seismological features on simulated data. However, there is a lack of knowledge about the main statistical features related to directivity effects on a more extended dataset depending on the earthquake scenarios and frequency intervals, which are important insights to empirically model ground shaking and to provide more physical constraints to their final predictions. Our work thus aims to increase this knowledge by recognizing the statistical features

of directivity on the basis of a very dense dataset of records in Central Italy, which represents an almost unique natural laboratory for earthquakes occurring on normal faults.

With this aim, we analyze the empirical frequency and azimuthal dependence of directivity imprinted in the distribution of the residuals between the observed and predicted data. We employ a fully non-ergodic GMM, which is here calibrated on the Fourier Amplitude Spectra (FAS). The relaxation of the ergodic assumption represents a relevant step towards the empirical modeling of directivity, as it allows to remove all the systematic components of variability, related not only to the event and site, but also to the source-to-site path and source region. It thus leads to better isolating the directivity contribution in the random term of the remaining residuals. The approach is entirely based on empirical observations, thanks to the large amounts of high-quality seismic recordings following the two main seismic sequences of L'Aquila in 2009 (Chiarabba et al., 2009; Walters et al., 2009) and Amatrice-Norcia in 2016 and 2017 (Chiaraluce et al., 2017; Pizzi et al., 2017).

The paper is outlined as follows: firstly, the dataset and the ground motion model used for the analysis are introduced, then directivity effects are modelled through an empirical approach based on residual decomposition, and the results are statistically analyzed. Finally, the main parameters controlling the phenomenon are identified for their potential implementation within ground motion predictive models in the field of engineering seismology such as for shaking scenarios and hazard assessments.

2 Dataset

The dataset is the same as used by Sgobba et al. (2021) and consists of high-quality accelerometric and velocimetric waveforms related to stations and earthquakes located in Central Italy since 2008. The tectonic setting of this region is complex in terms of mechanical discontinuities and rheological properties (Carafa and Barba, 2011; Chiarabba et al., 2018), featuring mainly normal faults that caused several seismic sequences in the last 20 years (i.e. 1997-1998, Umbria-Marche Mw 6.0; 2009, L'Aquila Mw 6.1; 2016-2017, Amatrice-Visso-Norcia Mw 6.5; 2018, Muccia Mw 4.6).

Fig. 1a shows the high density of events and stations in the study region, allowing a dense azimuthal sampling of source-to-site ray paths. The overall dataset analyzed in this study consists of more than 30'000 waveforms of 456 earthquakes in the magnitude range between 3.2

and 6.5, and 460 stations within 120 km from the epicenter (**Fig. 1b**). The bulk of data is included in the magnitude range 3.5-5.5 and in the distance interval 20-120 km, with some events recorded by over 100 stations.

Starting from this dataset, the study is conducted on the Fourier spectra of the portion of the signal containing the S-phases. For each record, we use a distance-dependent energy criterion to identify S-wave time window (Pacor et al., 2016b). As time windows of records close to the epicenter could be very short (generally less than 2 s), we fix a minimum length of 4 s in order to guarantee an acceptable spectral resolution above 1 Hz for the shortest windows. The extracted signals are tapered using Hanning windows with variable lengths, depending on the selected S-waves portion. Pre-event noise windows of the same length as the signal windows are used to compute the SNRs and a threshold equal to 3 is selected to remove noisy spectral ordinates.

3 Method

3.1 Non ergodic ground motion model

The proposed GMM is developed for the geometric mean of horizontal peak ground accelerations (PGA) and 69 FAS ordinates in the frequency range logarithmically equispaced from 0.5 to 25 Hz. The model is calibrated via a mixed-effect regression (Bates, 2015), providing the estimation of the different repeatable effects on the seismic motion (i.e. source, site and path), along with the associated aleatory variability.

We assume the same functional form proposed by Sgobba et al. (2021) for the response spectrum to describe PGA and spectral ordinates, Y, at each frequency $Y(f)$:

$$log_{10}Y = a + F_M(M) + F_R(M,R) + \delta B_e + \delta S2S_{ref,s} + \delta L2L_{source} + \delta P2P_p + \delta W_0 \quad [1]$$

where a, $F_M(M)$, $F_R(M,R)$ represent the fixed effects, and δB_e, $\delta S2S_{ref,s}$, $\delta L2L_{source}$, $\delta P2P_p$ stands for zero-mean gaussian-distributed random effects. Parameter a is the offset and F_M describes the scaling with magnitude:

$$F_M(M) = b_1(M_w - M_h) \text{ for } M \leq M_h,$$
$$F_M(M) = b_2(M_w - M_h) \text{ otherwise.} \quad [2]$$

Here b_1 and b_2 are calibrated coefficients, while M_h is the hinge magnitude fixed at 5.0. The term $F_R(M,R)$ is the other fixed term and represents the scaling with distance:

$$F_R(M,R) = \left[c_1\left(M_w - M_{ref}\right) + c_2\right] log_{10}\frac{\sqrt{R^2+h^2}}{R_{ref}} + c_3(\sqrt{R^2+h^2} - R_{ref}). \quad [3]$$

$F_R(M,R)$ is divided into a contribution due to the geometrical spreading (including magnitude-dependent with coefficient c_1, and magnitude-independent with coefficient c_2, terms) and the anelastic attenuation (described by c_3). M_{ref} is the reference magnitude set to 5.0, R_{ref} is the reference distance fixed at 1 km, h is the pseudo depth fixed at 6 km, and R is the Joyner-Boore distance for events larger than 5.5, for which the fault geometry was defined. For lower magnitude events, the Joyner-Boore distance is assumed to be equal to the epicentral distance, since the small area of the rupture surface makes the event equivalent to a point-like source.

The random error terms with respect to the median prediction of the GMM in equation [1] are as follows:

- δB_e is the between-event error, which corresponds to the average bias of recordings of one particular earthquake;
- $\delta S2S_{ref,s}$ is the site-to-site term, defining the systematic bias of ground motions recorded at each station;
- $\delta L2L_{source}$ is the source term, describing the systematic bias of the source regions;
- $\delta P2P_p$ is the path-term, denoting the systematic deviation along each source-to-site path (from each identified source region to the sites).

The source regions that are necessary for the computation of systematic terms $\delta L2L_{source}$ and $\delta P2P_p$ were defined by Sgobba et al. (2021) by performing a spatial-temporal clustering of the events in the dataset. In particular, these authors identified 6 clusters, 3 of these are located inside our study area (red box in **Fig. 1a**) and are shown in **Fig. 2**. These 3 clusters are (from South to North): cluster #1, including the 6 April 2009 Mw 6.1 L'Aquila, cluster #2, with the 2016 Mw 6.0 Amatrice and Mw 6.5 Norcia sequence, and cluster #3, including 2018 Mw 4.6 Muccia sequence.

One of the advantages of using a non-ergodic GMM with respect to the ergodic assumption is the removal of effects due to the different characteristics of the sources, site effects not modelled in the GMM, or isotropic and anisotropic path effects.

As a result, the leftover residuals δW_0 reflect the remaining variability unaccounted by Equation [1], which should represent the purely random term. However, this term could still include non-systematic effects related to the source-site configurations, such as the rupture-directivity, radiation pattern, slip patch distribution, etc. In the following, owing to the extensive coverage of the present dataset, we investigate the azimuthal dependence of the δW_0 terms to recognize a potential signature of source directivity effects.

3.2 Azimuthal variations of the $\delta W_0(\theta)$ residuals

For each event of the dataset and for each frequency, we analyze the azimuthal variation of the aleatory residuals δW_0. As an example, **Fig. 3** displays the spatial distribution of the PGA aleatory residuals for two M4 events of 30 October 2016 at 11:58:17 (**Fig. 3a**) and 31 October 2016 at 07:05:44 (**Fig. 3b**), both belonging to the 2016-2017 sequence in Central Italy.

Fig. 3a shows a clear spatial pattern with positive values of δW_0 to the South with respect to the epicenter and a well-defined azimuthal distribution (**Fig. 3c**), with peak amplitude of 0.6 at around 180°. Conversely, for the event plotted in **Fig. 3b** the distribution of δW_0 values, ranging between -0.4 and 0.4, are rather random without any predominant direction (**Fig. 3d**). The trend of the aleatory residuals relative to the same events of **Fig. 3** for 4 selected stations, each one located in a different quadrant is plotted in **Fig. 4**.

For the event of 30 October 2016 (**Fig. 4a**), we observe that the station FIAM, located south of the epicenter, is characterized by positive residuals, while MMUR, lying in the northern sector, is affected by negative residuals on the entire frequency range of investigation. The remaining two stations (MCIV and T1241), located in the eastern and western sectors, have similar trends with values spanning around zero. In contrast, for the event 31 October 2016 (**Fig. 4b**), no significant variations of the δW_0 can be distinguished from the 4 investigated stations. In the whole considered dataset, the cases above are only two illustrative examples, but we have several earthquakes which show different behavior of δW_0 with respect to the frequency: some of these events are shown in **Fig. S1**.

These observations are consistent with directivity effects that can generate spatial patterns, with the largest ground motion amplitude at sites located in the forward-direction with respect to the rupture propagation (Aki and Richards, 1980; Somerville et al., 1997). In light of this, the 30 October 2016 earthquake of **Fig. 3a** and **Fig. 3c** may be classified as a unilateral rupture event, where FIAM station is in the forward-directivity direction, MMUR in the backward-directivity direction, whereas MCIV and T1241 are in neutral positions. Conversely, the event on 31 October 2016 may be classified as a bilateral-rupture event without pronounced source directivity effects.

3.3 Directivity models for $\delta W_0(\theta)$

In order to detect and quantify the directivity effects from the aleatory residuals δW0, we introduce the following model:

$$\delta W_0 = \delta D2D(\theta) + \delta W_{nodir}, \quad [4]$$

where $\delta D2D(\theta)$ is the function that fits the residuals δW_0 for each event in the dataset as a function of the source-to-site azimuth θ, while δW_{nodir} are the remaining residuals cleared of the directivity effect. Two functional forms are adopted to describe the dependence on θ of the $\delta D2D$ term:

i. A cosinusoidal function selected on the basis of the trend of residual distribution with the azimuth θ of the sites (Somerville et al., 1997):

$$\delta D2D(\theta) = A cos(\theta - \theta_0), \quad [5]$$

where A is the amplitude of the fitting cosine function and θ_0 represents the azimuth at the maximum amplitude.

ii. The directivity coefficient C_d based on a simple theoretical rupture propagation model (Ben-Menahem, 1961; Ruiz et al., 2011; Pacor et al., 2016a; Gallovič, 2016), which is introduced to account for the rupture propagation on the fault plane. According to Boatwright (2007), the general expression of C_d for a bilateral rupture is the following:

$$C_d = \sqrt{\frac{k^2}{\left[1-\left(\frac{v_r}{c}\right)cos(\theta-\theta_0)\right]^2} + \frac{(1-k)^2}{\left[1+\left(\frac{v_r}{c}\right)cos(\theta-\theta_0)\right]^2}}, \quad [6]$$

where $\frac{v_r}{c}$ is the Mach number (ratio between rupture and shear-wave velocities, denoted as α in the following), while θ and θ_0 are the azimuths related to the station and to the rupture direction, respectively. Parameter $k \in <0;1>$ represents the relative portion of the rupture length in the direction θ_0.

In the case of a unilateral rupture propagating along a narrow fault at a constant velocity v_r, k is equal to 1 and the full expression of C_d reduces to that for the Haskell (1964) model:

$$C_d = \frac{1}{1-(\frac{v_r}{c})cos(\theta-\theta_0)} \quad [7]$$

Corner frequencies for sites affected by directivity are given by the apparent corner frequency $f_a = f_c C_d(\theta)$, where f_c is proportional to the reciprocal of the rupture duration. The amplitude of the source spectral ordinates scale proportionally to C_d^n above frequency f_a, where the exponent n depends on the type of the source model. Omega-squared kinematic rupture models with single corner frequency (e.g., k-squared model by Herrero and Bernard, 1994) suggest $n = 2$, while models with two corner frequencies (e.g., Haskell model, with constant slip and rise time) suggest $n = 1$. In case of purely stochastic models, the directivity disappears and n becomes null (see Gallovič, 2016).

In this second approach, the corrected event-site and path residuals of **Eq. 4** are fitted by the following function for each frequency:

$$\delta D2D(\theta) = log_{10}C_d^n(\theta) - <log_{10}C_d^n(\theta)>, \quad [8]$$

where $<>$ denotes azimuthal averaging. The fitting variables are the angle of the rupture direction θ_0, the ratio k, the Mach number α and the exponent n.

3.4 Tuning of model parameters

In order to determine the fitting parameters, we calibrate the C_d model using the Levenberg-Marquardt optimization algorithm (Marquardt, 1963), which is commonly adopted to solve non-linear least squares problems. In the optimization tests, we assume that the explanatory parameters

vary within a fixed range of values: n spans in the interval between 0 and 2, k between 0.6 and 1, α from 0.5 to 1 and θ_0 in the range 0-360°.

While the fitting of the cosine function is straightforward (Sgobba et al., 2021), the choice of variables in **Eq. 6** should be evaluated considering a strong trade-off among some of the fitting parameters. In particular, as already shown in Pacor et al. (2016a), similar fitting functions are obtained for different combinations of α and n. An investigation by Ren et al. (2017), for instance, suggests that the optimum Mach number α can vary in a range from $\sim$0.5 to $\sim$1.0, and strongly depends from the value of exponent n considered, as smaller values of n typically result in larger values of the Mach number.

In **Fig. 5** and **Tab. 1**, we show an example of the fitting of the residuals for the event of **Fig. 3a**, which is obtained at three different frequencies (results for other sample events are reported in **Fig. S2**).

In general, the fit with fixed values $k = 0.85$ and $\alpha = 0.5$ (blue curve in **Fig. 5** and case III in **Tab. 1**) has the best performance in the majority of the cases being able to also capture the trend of the residuals also in the anti-directive azimuths. The goodness of fit is evaluated through the coefficient of determination R^2 which is a robust statistical measure of relationships between 2 variables. Since these values ($k = 0.85$ and $\alpha = 0.5$) are also found to be consistent with common seismological observations (Ren et al., 2017), we decide to adopt this fitting function for the final C_d model.

In **Fig. 6** we highlight the trend of the directivity parameters as a function of frequency for the two events shown in **Fig. 3**. Other examples are reported in **Fig. S3**.

For the M4.0 event of 30 October 2016 at 11:58:17, the directivity amplifications is larger than 0.2 and 0.4 if we observe the amplitude A from cosine fitting (black curve) and the value of n (blue curve) from the C_d model, respectively (**Fig. 6a** at the top). In particular, if we look at C_d model, we find a maximum around 5 Hz with values of n close to 1. The direction of the rupture propagation does not change with frequencies (**Fig. 6a** in the middle), while the coefficient of determination R^2 follows the frequency trend of the amplification level and thus can be considered a *proxy* of the significance of the directivity effects in the ground motions. The M4 event of 31 October 2016 (**Fig. 6b**) shows instead small amplification (< 0.4) at all frequencies both for cosine and C_d models, the θ_0 has a random trend and R^2 is consistently below 0.5, indicating that no directivity occurs for this event. Although the simple cosine model adequately describes the

residuals, we prefer the C_d model in the subsequent analyses, since it is more related to the physics of the phenomenon.

In particular, we observed that the C_d function provides a better description of the azimuthal variation of the residuals compared to the simpler cosinus-type relationship as it reproduces better the asymmetry observed in ground motion amplification of directive sites and the de-amplification of non-directive sites.

4 Results

We apply the above-described method to all the events of the dataset. About 10% of the investigated events (47 out of 456 events) is characterized by a coefficient of determination R^2 and exponent n (median over the frequency-range) less than 0.25 and 0.3, respectively, thus indicating that the directivity is negligible. For all the other events, the phenomenon of directivity is present with variable intensity in different frequency bandwidths (see examples for Mw between 3.7-4.0 in **Fig.7**). In general, the coefficient of determination R^2 and the value of the exponent n for the function C_d are strongly correlated (Pearson coefficient ρ is always greater than 0.7 and, for frequency values greater than 1 Hz, greater than 0.9), as shown by the graph of the correlation coefficient computed for each frequency analyzed in this study (see **Fig. S4**). Since in this research we want to focus on directive events only, we introduce a selection criteria described in the following section.

4.1 Identification of events with significant directivity

Considering that for each event the phenomenon of directivity exhibits itself with variable intensity in different frequency bands of variable length (**Fig. 7**), we introduce some assumptions for identifying a directive event. We designate an event as directive if:

i) The coefficient of determination R^2 is greater than 0.5 (with a tolerance of 0.05) for at least 10% of the frequencies investigated (in our case, 7 out of 69 values).

ii) The standard deviation of the angle of the direction of propagation θ_0 is smaller than 20° in the same frequency range.

Fig. 7 shows the values of n as a function of the frequencies analyzed for each event within the magnitude range between 3.7 and 4.0 (for the behavior of n with respect to the other magnitude classes, see **S5**). Since the frequency ranges analyzed are logarithmically equispaced, the upper part of the graph on x-axis shows the log_2 of the frequency, while the corresponding value of the

frequency content is shown at the bottom of the x-axis. After the selection criteria, in order to guarantee the continuity of the frequency-bandwidth with respect the physics of the phenomenon, eventual gaps (composed with less than 5 consecutive frequency intervals) are filled with the average values in the missing frequency ranges, providing the condition with $R^2 > 0.45$ for closing the gap.

4.2 Directivity event distributions

According to the criteria defined in 4.1, about 36% of the analyzed earthquakes (162 out of 456) can be classified as directive. **Table S1** provides a list with all the characteristics of the directive events (ID of the event, Latitude, Longitude and magnitude), including the frequency bandwidth where the directivity criterion is satisfied.

The number of the directive events seems independent of magnitude, being distributed as the entire dataset, as illustrated by the histograms reported in **Fig. 8a**.

Fig. 8b shows the percentage of directive events as a function of frequency for different magnitude ranges (black lines, all events). At low frequencies, this percentage is less than 6% of the total, then increases to about 20% in the range 5-10 Hz and finally reduces to 10% at higher frequencies. The same trend is visible for events smaller than 4.1 (green and blue lines in **Fig. 8b**), that represent the bulk of the catalogue.

As the magnitude increases, these effects start to shift to lower frequencies, although the trends are more scattered due to the reduction of the events. Indeed, directivity for moderate events (magenta and blue curves in **Fig. 8b**) is mainly observed at intermediate frequencies in the band 5-10Hz. For events with magnitude greater than 5 (magenta curve in **Fig. 8b**), more than 30% of the total events exhibit remarkable directivity mainly at lower frequencies (f $\leq$ 1 Hz), while this percentage drops starting from 2 Hz.

4.3 Directivity frequency band

As clearly observed in **Fig. 7** and also broadly discussed in other works (Chen et al., 2014; Pacor et al., 2016a; Hirano and Yagi, 2017), the directivity occurs in variable frequency bands that may depend on the magnitude of the event. To this purpose, from each directive event of the dataset listed in **Table S1**, we estimate the minimum f_{min} and the maximum frequencies f_{max} corresponding to the values where $R^2 > 0.5$ and plot them as a function of magnitude in **Fig. 9**. There, we also report the corner frequency f_c (blue stars) of the events, estimated by Bindi et al. (2018) applying a generalized spectral inversion technique (GIT) to a similar dataset in Central

Italy. What we can observe is that, in agreement with the basic theoretical consideration, the corner frequency represents a lower bound below which directivity cannot occur (Motazedian and Atkinson, 2005; Chen et al., 2014; Pacor et al., 2016a).

In order to highlight the dependencies among the various frequencies and magnitude, we plot in **Fig. 9** the median values computed on the half-magnitude bins. While the scatter between f_{min} and f_{max} is relatively large (red and green symbols in **Fig. 9**), binned median values (red and green solid lines in **Fig. 9**) exhibit a decaying trend with increasing magnitude. The decay rate is roughly similar to that of the corner frequency, suggesting a relation of the directivity bandwidth on the source properties (Trugman et al., 2021). Frequencies f_{min} and f_c assume approximately the same values for events with magnitude greater or equal than 4 (although they are only a small proportion of the total events), while for smaller magnitudes the relationship between $log_2 f_{min}$ and $log_2 f_c$ seems constant and equal to about 1.6 log_2 units.

In particular, the directivity bandwidth, defined by the ratio between $\frac{f_{max}}{f_{min}}$ in log_2 scale (i.e., number of octaves), is similar for both small and moderate events. This bandwidth is, on average, to about 2.3 octaves (i.e. $\frac{f_{max}}{f_{min}} \sim 5$), although this observation may be masked by the limited number of events with M > 4 and the maximum frequency of the dataset set at 25 Hz.

This factor is estimated *ad-hoc* for the Central Italy dataset, but there are also theoretical reasons for having the directivity effect scale-dependent. In fact, as pointed out in Pacor et al. (2016a), it seems reasonable that at short scales (~5-7 times smaller wavelengths than the rupture size), the rupture propagation is complex, not exhibiting coherent rupture propagation in a single direction. Similarly, the wave propagation due to the complexities of the 3-D velocity model may play a significant role in destroying the directivity effect with the seismic waves coming from various parts of the fault becoming less coherent with increasing frequency.

4.4 Directivity amplitude

As mentioned before, the value of n depends on the type of source model considered, ranging from 0, which represents an incoherent not-directive rupture, to 2, which corresponds to a coherent rupture with the strongest directivity effect. For each event analyzed in this work, we take into account both the peak value n_{max} and the median value n_{med}, computed within the frequency band where $R^2 > 0.5$.

As we can observe from the histograms of **Fig. 10**, the median values n_{med} span between 0.26 and 2.1 (median 0.69, mean 0.77), while the maximum values n_{max} vary from 0.8 to 2.8 (median 1.4, mean 1.44). We also note that the largest values of n (above 2) can be alleviated by considering larger rupture velocity (i.e. Mach number) in the fitting procedure. The amplitude of directivity is independent of magnitude, but shows a rather evident linear correlation with the bandwidth of the directivity effects (**Fig. 11**). In particular, the higher is the value of n_{med}, the wider is the frequency band where directivity is observed (in **Fig. S6**, the plot for n_{max} is reported), although the dispersion increases.

As shown in **Fig.11**, the linear fit between n_{med} and the ratio $\frac{f_{max}}{f_{min}}$ in logarithmic scale (base 2), is established by the relation:

$$log_2 \frac{f_{max}}{f_{min}} = 2.7427 * n_{med} - 0.1457 \quad [9]$$

The correlation coefficient r, which measures the strength of the linear relationship between n_{med} and bandwidth is 0.7607.

4.5 Direction of rupture propagation

In **Fig. 12,** we show the median value of the direction of rupture propagation, θ_0, for the events with directivity. The distribution is bimodal with two peaks around 150° (SE) and 330° (NW), which are aligned with the fault strikes of the Central Apennines events (D'Amico et al., 2013; Tinti et al., 2016; Improta et al., 2019; Vignaroli et al., 2020).

We try to find a possible relation between the preferential rupture direction and seismogenic areas or elements connected to the structural geology. We first consider division into source areas following the cluster classification of Sgobba et al., 2021 (**Fig. 2)**, and we do not find any preferred rupture direction. After that, we consider a division based on the recent results from the RETRACE-3D project (Di Bucci et al., 2021, www.retrace3d.it) focused on the revision of all the available geological and geophysical data in the area of the 2016-2018 Central Italy seismic sequence.

In particular, we take into consideration one of the major geological structures of the Central Apennines, the Sibillini thrust system (**Fig. 13a**), which consists of a west-dipping, regional ramp-

423 flat structure over thrusting (Lavecchia, 1985; Pierantoni et al., 2013; Porreca et al., 2018) and
424 divides the investigated zone in the hanging and footwall areas to the north and south, respectively.
425 According to Pizzi et al. (2017), the Mt. Sibillini thrust played a key role as a structural barrier at
426 depth, controlling the rupture of the Mw 6.2 Amatrice event of 24 August 2016 (Chiaraluce et al.,
427 2017) and the initiation of the Mw 6.5 Norcia mainshock of 30 October. In particular, the area
428 struck by the Mw 6.5 seismic sequence has a geo-structural architecture delimited to the East by
429 the deep portion of the Miocene-Pliocene Sibillini thrust system, which according to Buttinelli et
430 al. (2021) is the fault that better matches the hypocentral depth and average rupture dip of the Mw
431 6.5 mainshock.

432 In general, about 60% of the events lie in the cluster at the North to the Mt. Sibillini, while the
433 remaining ones belong to the hanging wall. Histograms in **Fig. 13b** and relative maps in **Fig. 13c**
434 and **Fig. 13d** suggests that for the hanging wall, the events have a fairly equal distribution of
435 unilateral propagation towards North-West and South-East. With regards to the earthquakes lying
436 in the footwall, we found a preference of the northward direction of the rupture propagation (44
437 vs 19 events at the cluster North and South equivalent to about 70% and 30%, respectively). This
438 preferential northward direction of the footwall, that are evident in particular from the aftershocks
439 of the L'Aquila and Amatrice-Visso-Norcia sequences, is in agreement with the findings of
440 Calderoni et al. (2015) and Calderoni et al. (2017), respectively, who investigated the source
441 directivity analyzing the azimuthal variation of records by means of the spectral ratio technique.

442 **5 Discussion**

443 In the following, we introduce a first-order classification of the directive events, based on the
444 relations among the frequency bandwidth $\Delta f = log_2 \frac{f_{max}}{f_{min}}$, the amplitude, proportional to n_{med} and
445 the minimum frequency f_{min} at which directivity occurs.

446 To this aim, we plot the distribution of the events on a f_{min} - Δf graph (**Fig. 14**), where each
447 data point is colored in function of the values of n_{med}. To group data-point in classes,
448 representative of the "strength" of directivity, we identify three threshold levels, following the
449 n_{med} distribution reported in **Fig. 10**. The *weak-directivity* class is relative to $n_{med} < 0.8$
450 (corresponding to the 65th percentile of the distribution), the *moderate-directivity* class is in the

range between 0.8 and 1.3 (around 65th and 95th percentiles) and *high-directivity* class is given by n_{med} > 1.3.

One can observe in **Fig. 14** that these three classes are not randomly distributed, but are localized on specific portions of the graph: the weak directivity events are mainly in the bottom part, the moderate ones in the middle, and the high ones lie on the top. This pattern suggests the definition of three domains, delimited by different values of directivity amplitude and frequency bandwidth. The limiting values of Δf are set to the 75th percentile of the corresponding distributions evaluated for each of the three directivity classes, for which we assumed that the median amplitude n_{med} is uniformly distributed over the frequency range.

As we can observe in **Fig. 14**, the first domain is characterized by weak-directivity and small values of Δf, extended up to 1.8 octaves (i.e. *narrow band*), the second one is a "transition" zone, up to 3.4 octaves, formed by the majority of events with moderate directivity and intermediate values of Δf up to 3.4 octaves and a third zone (> 3.4 oct), where we mainly find events characterized by high-directivity and larger Δf (*broadband*).

Such a pattern seems to confirm the existence of a physical correlation between the frequency bandwidth and the strength of directivity so that more directive events tend to show broadband features in contrast to weaker ones that are more bounded in frequency. It is worth to be noted, however, that these findings are strictly related to the statistics of the investigated dataset for Central Italy and that we are also limited in exploring the directivity strength of the smallest events due to the inherent limit of observation, which reaches up to a maximum frequency of 25 Hz (the unexplored domain is displayed with a grey triangle with mesh net in **Fig. 14**).

As an example of application, we consider a scenario earthquake with Mw 4.6 in the study area. Following the seismological relation by Morasca et al. (2019) calibrated for Central Italy, this magnitude corresponds to a corner frequency f_c approximately equal to 1 Hz, that can be assumed equal to f_{min} according to the trend illustrated in **Fig. 9**. Based on the above findings, this f_{min} may correspond to different frequency bandwidths according to the level of n_{med} (black dashed lines in **Fig. 14**). For instance, an event with weak-directivity (n_{med}=0.55) is characterized by a directivity bandwidth ranging from f_{min} equal to 1 Hz up to 3 Hz, being Δf=1.55 octaves according to **Eq. 9**. On the other hand, for an high-directivity event with n_{med}=1.55, we get a

value of bandwidth Δf=4.1 octaves (red cross in **Fig. 14**), which means that in this case directivity appears from 1 to about 18 Hz.

6 Conclusions

In this work we have shown a statistical overview aiming to provide a better understanding of the main features of the rupture directivity based on empirical evidence of seismological observations. The study exploits the exceptionally dense dataset of Central Italy compiled after the main sequences of L'Aquila in 2009 and Amatrice-Visso-Norcia from 2016 to 2018 with a large number of recordings and broad azimuthal coverage.

We take advantage of this dataset to calibrate an *ad-hoc* fully non-ergodic FAS-GMM adopted as a reference model for the target area. The non-ergodicity enables to remove all the other components of variability (i.e. the event-, site- and path-related) in the ground motion model and hence allowing to better isolate the effects related to source-directivity, that are not unaccounted in the epistemic variability of the GMM.

The aleatory residuals of such a model exhibit a clear azimuthal pattern and a frequency dependence, which represents the signature of source directivity, in line with previous studies (Pacor et al., 2016a; Luzi et al., 2017; Sgobba et al., 2021). We found that the residuals are well fitted and modelled by the directivity function $C_d^n(\theta)$ that allows us to capture the empirical pattern in a physically-consistent manner and to link the observations with the main parameters related to the earthquake rupture propagation. Moreover, this function is capable of reproducing the asymmetry observed in ground motion amplification of directive sites and the de-amplification of non-directive sites in a more effective way than the simple cosine function.

The physics-based parameters in the $C_d^n(\theta)$ fitting function are the Mach number α (ratio between the rupture velocity and the shear-wave velocity), the k parameter (the portion of the rupture length in the propagation direction) and the angle θ_0, which define the direction of the rupture propagation. The strength of the azimuthal variability of ground motions is proportional to the exponent n, and thus it is a parameter representative of the "strength" of the directivity (having interpretation in theoretical kinematic rupture models). Optimization tests confirmed the existence of a strong trade-off among the directivity parameters. We therefore fixed some of them at typically

accepted values in seismological applications: $k = 0.85$, $\alpha = 0.5$ with θ_0 free to vary but generally assuming values around 150°, in line with the fault strikes of the Central Apennines. In particular, we prefer to allow n to possibly depend on frequency, as it is theoretically more acceptable than frequency dependence of the rupture velocity.

Once fixed the main parameters, the statistical investigation performed on the whole dataset evidences different directivity intensity levels on ground motion, which reflect in terms of different values of the exponent n. On this basis, we classify the events in the dataset as "directive" and "non-directive" as a function of a statistical *proxy*, i.e. the coefficient of determination R^2, assuming that the directivity effect is relevant when the R^2 associated is greater than 50%. Grounding on this main assumption, we found that:

- The azimuthal distribution of the directive events, which in our analysis corresponds to the 36% of the whole dataset, is bimodal with two peaks (i.e. the most frequent orientations in the dataset) at 150° and 330°, corresponding to the NW-SE alignment of the Central Apennines fault systems. This finding suggests that the azimuthal orientation of directivity is regional-dependent and relates to geological and structural settings of the area.

- A preferential direction of directivity is not clearly dominant in the whole dataset. We observed that the Amatrice sector (cluster South) is more affected by a predominant propagation towards N-NW (70%) against 30% towards S-SE. Conversely, the events in cluster North, corresponding to the Norcia sector, do not show a preferential direction, thus resembling a random pattern. These results suggest that the main structural discontinuity of the region (i.e. the Mt. Sibillini thrust) may produce distinctive features in the directivity pattern depending on the location of the nucleation rupture point, hence being likely related to rheological and structural properties, as shown also by Calderoni et al. (2017) with the events of 2016-2017 seismic sequence of Central Italy. However, the present results need more extensive correlations with rheological parameters to be confirmed.

- The observed directivity is a band-limited phenomenon: it occurs always above the corner frequency, up to a maximum value (f_{max}) approximately equal to about 5 times the

minimum frequency (f_{min}) at which the proxy R^2 becomes significant (i.e. larger than 50%). However, we have to take into account that the f_{max} may be underestimated, especially for small events, since the maximum frequency investigated in our study is 25 Hz. Moreover, since we do not have complete information of the source parameters for small-magnitude earthquakes (e.g. stress drops are intrinsically difficult to estimate for M < 4, see Abercrombie et al., 2021), we could not observe a dependence of magnitude on directivity bandwidth for each event examined.

The latter point we touched may represent a first step towards the empirical parameterization of directivity effects, since it connects the persistence of directivity at some frequencies with the fundamental scenario's parameters. In fact, we could combine together the main statistical outcomes of this study to use the directivity function $C_d^n(\theta)$ for predictive purposes, by setting k and α (due to their trade-off with n) along with θ_0 variables and then computing the stress drop and corner frequency using seismological scaling laws from the input magnitude.

This effort to incorporate the directivity contributions into empirical GMMs was carried out because past investigations performed in the NGA-West2 project (Spudich and Chiou, 2008; Spudich, 2014) led to the conclusion that 'none of these models has a functional form that transitions smoothly from large to small magnitude and that describes the small-magnitude or short-period directivity'. Our results in this sense may provide useful insights to move towards parametrization of directivity within the empirical simulation of shaking scenarios in Central Italy, as the ones proposed by Sgobba et al. (2021) in the non-ergodic framework. However, we clarify that the proposed approach reproduces well the characteristics of the data in the target region while more extensive research is needed to generalize these findings.

Acknowledgements

We are very grateful to Prof. Daniele Spallarossa (University of Genova, Italy) for making the dataset used in this work available. This research is supported by *Istituto Nazionale di Geofisica e Vulcanologia* (INGV) in the frame of the project *Pianeta Dinamico* (Working Earth) - Geosciences for the Understanding of the Dynamics of the Earth and the Consequent Natural Risks (CUP code D53J19000170001), founded by the Italian Ministry of University and Research (MIUR) in the Task S3 - 2021 - Seismic attenuation and variability of seismic motion. Moreover, this study has been partially funded by INGV-DPC Agreement B1 2019-2021, with the goal of promoting research activities in the field of seismic hazard in Italy. All the authors declare that the research was conducted in the absence of any commercial or financial relationships that could be construed as a potential conflict of interest.

References

Abercrombie, R. E., Poli, P., and Bannister, S. (2017). Earthquake directivity orientation, and stress drop within the subducting plate at the Hikurangi margin, New Zeland. *J. Geophys. Res. Solid Earth, 122,10, 176-10, 188*. 4. https://doi.org/10.1002/2017JB014935.

Abercrombie, R. E., Trugman, D. T., Shearer, P. M., Chen, X., Zhang, J., Pennington, C. N., Hardebeck, J. L., Goebel, T. H. W., and Ruhl, C. J. (2021). Does earthquake stress drop increase with depth in the crust? *J. Geophys. Res. Solid Earth, 126, 10.* https://doi.org/10.1029/2021JB022314.

Aki, K., and Richards, P., 1980. Quantitative Seismology: Theory and Methods. W. H. Freeman.

Ameri, G., Massa, M., Bindi, D., D'Alema, E., Gorini, A., Luzi, L., Marzorati, S., Pacor, F., Paolucci, R., Puglia, R., and Smerzini, C. (2009). The 6 April 2009 Mw 6.3 L'Aquila (Central Italy) Earthquake: strong-motion observations. *Seismol. Res. Lett*., 80 (6), 951-966. https://doi.org/10.1785/gssrl.80.6.951.

Anderson, J. G. (2007). Earthquake Seismology - Physical processes that control strong ground motion. In *Treatise on Geophysics, 2nd Edition.* Elsevier.

Bates, D., Mächler, B., Bolker, B., and Walker, S. (2015). Fitting linear mixed-effects models using lme4, 2015. *J. Stat. Software*, 67(1), 1-48. https://doi.org/10.18637/jss.v067.i01.

Ben-Menahem, A. (1961). Radiation of seismic surface waves from finite moving sources. *Bull. Seismol. Soc. Am., 51*, 401- 435.

Bernard, P., and A. Herrero (1994). Slip heterogeneity, body-wave spectra, and directivity of earthquake ruptures. *Ann. Geofis., 37*, 1679-1690. https://doi.org/10.4401/ag-4159.

Bernard, P., Herrero, A., and Berge, C. (1996). Modelling directivity of heterogeneous earthquake ruptures. *Bull. Seism. Soc. Am., 86*, 1149-1160. https://doi.org/10.1785/BSSA0860041149.

Bindi, D., Spallarossa, D., Picozzi, M., Scafidi, D., and Cotton, F. (2018). Impact of Magnitude Selection on Aleatory Variability Associated with Ground-Motion Predictions Equations: Part I - Local, Energy, and Moment Magnitude Calibration and Stress-Drop Variability in Central Italy. *Bull. Seismol. Soc. Am., 108(3A)*, 1427-1442. https://doi.org/10.1785/0120170356.

Boatwright, J., (2007). The persistence of directivity in small earthquakes. *Bull. Seismol. Soc. Am., 97,* 1850-1861. https://doi.org/10.1785/0120050228.

Buttinelli, M., Petracchini, L., Maesano, F. E., D'Ambrogi, C., Scrocca, D., Marino, M., Capotorti, F., Bigi, S., Cavinato, G. P., Mariucci, M. T., Montone, P., and Di Bucci, D. (2021). The impact of structural complexity, fault segmentation, and reactivation on seismotectonics: Constraints from the upper crust of the 2016-2017 Central Italy seismic sequence area. *Tectonophysics*, 810, 228861. https://doi.org/10.1016/j.tecto.2021.228861.

Calderoni, G., Rovelli, A., Ben-Zion, Y., and Di Giovambattista, R. (2015). Along-strike rupture directivity of earthquakes of the 2009 L'Aquila, Central Italy, seismic sequence. *Geophys. J. Int., 205*, 399-415. https://doi.org/10.1093/gji/ggv275.

Calderoni, G., Rovelli, A., and Di Giovambattista, R. (2017). Rupture directivity of the strongest 2016-2017 Central Italy earthquakes. *J. Geophys. Res. Solid Earth, 122(11),* 9118-9131. https://doi.org/10.1002/2017JB014118.

Carafa, M. C., and Barba, S. (2011). Determining rheology from deformation data: The case of central Italy. *Tectonics, 30 (2)*. https://doi.org/10.1029/2010TC002680.

Chen, P., Jordan, T. H., and Zhao, L. (2010). Resolving fault plane ambiguity for small earthquakes. *Geophys. J. Int., 181*, 493-501. https://doi.org/10.1111/j.1365-246X.2010.04515.x.

Chen, Y., Letort, J., Cotton, F., and Drouet, S. (2014). High-frequency directivity effects: evidence from analysis of the Les Saintes records. *J. Seismol.*, 18, 457-466. https://doi.org/10.1007/s10950-014-9419-2.

Chiarabba, C., Amato, A., Anselmi, M., Baccheschi, P., Bianchi, I., Cattaneo, M., Cecere, G., Chiaraluce, L., Ciaccio, M. G., De Gori, P., De Luca, G., Di Bona, M., Di Stefano, R., Faenza, L., Govoni, A., Improta, L., Lucente, F. P., Marchetti, A., Margheriti, L., Mele, F., Michelini, A., Monachesi, G., Moretti, M., Pastori, M., Piana Agostinetti, N., Piccinini, D., Roselli, P., Seccia, D., and Valoroso, L. (2009). The 2009 L'Aquila (Central Italy) Mw6.3 earthquake: Main shock and aftershocks. *Geophys. Res. Lett., 36*, L18308. https://doi.org/10.1029/2009GL039627.

Chiarabba, C., De Gori, P., Cattaneo, M., Spallarossa, D. and Segou, M. (2018). Faults Geometry and the Role of Fluids in the 2016-2017 Central Italy Seismic Sequence. *Geophys. Res. Lett. 45 (14),* 6963-6971. https://doi.org/10.1029/2018GL077485.

Chiaraluce, L., Di Stefano, R., Tinti, E., Scognamiglio, L., Michele, M., Casarotti, E.. Cattaneo, M., De Gori, P., Chiarabba, C., Monachesi, G., Lombardi, A., Valoroso, L., Latorre, D.,

633 and Marzorati, S. (2017). The 2016 Central Italy Seismic Sequence: A First Look at the
634 Mainshocks, Aftershocks, and Source Models. *Seismol. Res. Lett. 88 (3),* 757-771.
635 https://doi.org/10.1785/0220160221.
636 Chioccarelli, E. and Iervolino, I. (2014). Sensitivity analysis of directivity effects on
637 PSHA. *Boll. Geof. Teor. Appl., 55(1),* 41-53. https://doi.org/0.4430/bgta0099.
638 Convertito, V., Catalli, F., and Emolo, A. (2013). Combining stress transfer and source
639 directivity: the case of the 2012 Emilia seismic sequence. *Sci. Rep.* 3, 3114.
640 https://doi.org/10.1038/srep03114.
641 Convertito, V., Pino, N. A., and Di Luccio, F. (2016). Investigating source directivity of
642 moderate earthquakes by multiple approach: the 2013 Matese (southern Italy) Mw=5 event.
643 *Geophys. J. Int., 207,* 1513-1528. https://doi.org/10.1093/gji/ggw360.
644 Courboulex, F., Dujardin, A., Vallee, M., Delouis, B., Sira, C., Deschamps, A. Honore, L.
645 and Thouvenot, F. (2013). High-frequency directivity effect for an Mw 4.1 earthquake, widely felt
646 by the population in southeastern France. *Bull. Seismol. Soc. Am., 103,* 3347-3353.
647 https://doi.org/10.1785/0120130073.
648 D'Amico, S., Orecchio, B., Presti, D., Neri, G., Wu, W.-N., Sandu, I., Zhu, L. and
649 Hermann, R. B. (2013). Source parameters of small and moderate earthquakes in the area of the
650 2009 L'Aquila earthquake sequence (Central Italy). *Phys. Chem. Earth,* 63, 77-91.
651 https://doi.org/10.1016/j.pce.2013.02.005.
652 Di Bucci, D., Buttinelli, M., D'Ambrogi, C., Scrocca, D., and the RETRACE-3D Working
653 Group, (2021). RETRACE-3D project: a multidisciplinary collaboration to build a crustal model
654 for the 2016-2018 Central Italy seismic sequence. *Boll. di Geofis. Teor. ed Appl., 62(1),* 1-18.
655 https://doi.org/10.4430/bgta0343.
656 Douglas, A., Hudson, J. A., and Pearce, R. G. (1988). Directivity and the Doppler effect.
657 *Bull. Seismol. Soc. Am., 78 (3),* 1367-1372.
658 Gallovič, F. (2016). Modeling Velocity Recordings of the Mw 6.0 South Napa, California,
659 Earthquake: Unilatel Event with Weak High-Frequency Directivity. *Seismol. Res. Lett., 87(1),* 2-
660 14. https://doi.org/10.1785/0220150042.
661 Haskell, N. (1964). Total energy and energy spectral density of elastic wave radiation from
662 propagating faults. *Bull. Seism. Soc. Am., 54 (6A),* 1811-1841.

Herrero, A., and Bernard, P. (1994). A kinematic self-similar rupture process for earthquakes. *Bull. Seism. Soc. Am., 84(4),* 1216-1228. https://doi.org/10.1785/BSSA0840041216.

Hirano, S., and Yagi, Y. (2017). Dependence of seismic and radiated energy on shorter wavelength components. *Geophys. J. Int., 209*, 1585-1592. https://doi.org/10.1093/gji/ggx108.

Improta, L., Latorre, D., Margheriti, L., Nardi, A., Marchetti, A., Lombardi, A. M., Castello, B., Villani, F., Ciaccio, M. G., Mele, F. M., Moretti, M., and The Bollettino Sismico Italiano WG (2019). *Sci. Rep., 9,* 6921. https://doi.org/10.1038/s41598-019-43393-2.

Joyner, W. (1991). Directivity for non-uniform ruptures. *Bull. Seismol. Soc. Am., 81*, 1391-1395. https://doi.org/10.1785/BSSA0810041391.

Lavecchia, G. (1985). Il sovrascorrimento dei Monti Sibillini: analisi cinematica e strutturale. *Boll. Soc. Geol. Ital., 104*, 161-194.

López-Comino, J. A., Cesca, S., Niemz, P., Dahm, T. and Zang, A. (2021). Rupture Directivity in 3D Inferred From Acoustic Emissions Events in a Mine-Scale Hydraulic Fracturing Experiment. *Front. Earth. Sci. 9*: 670757. https://doi.org/10.3389/feart.2021.670757.

Luzi, L., Pacor, F., Puglia, R., Lanzano, G., Felicetta, C., D'Amico, M., Michelini, A., Faenza, L., Lauciani, V., Iervolino, I., Baltzopoulos, G., and Chioccarelli, E. (2017). The Central Italy seismic sequence between August and December 2016: analysis of strong-motion observations. *Seismol Res Lett., 88(5)*: 1219-1231. https://doi.org/10.1785/0220170037.

Marquardt, D. (1963). An Algorithm for Least-Squares Estimation of Nonlinear Parameters. In *SIAM Journal on Applied Mathematics. 11 (2)*, 431-441.

McGuire, J. J. (2004). Estimating finite source properties of small earthquake ruptures. *Bull Seismol Soc Am., 94(2)*, 377-393. https://doi.org/10.1785/0120030091.

Morasca, P., Walter, W. R., Mayeda, K., and Massa, M. (2019). Evaluation of earthquake stress parameters and its scaling during the 2016-2017 Amatrice-Norcia-Visso sequence - Part I. *Geophys J. Int.*, 218 (1), 446-455. https://doi.org/10.1093/gji/ggz165.

Motazedian, D., and Atkinson, G. M. (2005). Stochastic finite-fault modeling based on a dynamic corner frequency. *Bull. Seism. Soc. Am.*, *95*(3), 995-1010. https://doi.org/10.1785/0120030207.

Pacor, F., Cultrera, G., Mendez, A., and Cocco, M. (2005). Finite fault modeling of strong ground motions using a hybrid deterministic-stochastic approach. *Bull. Seism. Soc. Am., 95*, 225-240. https://doi.org/10.1785/0120030163.

Pacor, F., Gallovič, F., Puglia, R., Luzi, L., and D'Amico, M. (2016a). Diminishing high-frequency directivity due to a source effects: empirical evidence from small earthquakes in the Abruzzo region, Italy. *Geophys Res Lett.: Solid Earth, 43,* 5000-5008. https://doi.org/10.1002/2016GL068546.

Pacor, F., Spallarossa, D., Oth, A, Luzi, L., Puglia, R., Cantore, L., Mercuri, A., D'Amico, M., and Bindi, D. (2016b). Spectral models for ground motion prediction in the L'Aquila region (Central Italy): evidence for stress-drop dependence on magnitude and depth. *Geophys. J. Int.*, 204, 697-718. https://doi.org/10.1093/gji/ggv448.

Pierantoni, P., Deiana, G., Galdenzi, S. (2013). Stratigraphic and structural features of the Sibillini mountains, Umbria-Marche Apennines (Italy). *Ital. J. Geosci.,* 132 (3), 497-520. https://doi.org/10.3301/IJG.2013.08.

Pizzi, A., Di Domenica, A., Gallovič, F., Luzi, L., and Puglia, R. (2017). Fault segmentation as constraint to the occurrence of the main shocks of the 2016 Central Italy seismic sequence. *Tectonics, 36,* 2370–2387. https://doi.org/10.1002/2017TC004652.

Porreca, M., Fabbrizzi, A., Azzaro, S., Pucci, S., Del Rio, L., Pierantoni, P. P., Giorgetti, C., Roberts, G., and Barch, M. R. (2020). 3D geological reconstruction of the M. Vettore seismogenic fault system (Central Apennines, Italy): Cross-cutting relationship with the M. Sibillini thrust. *J. Struct. Geol*., 131, 103938. https://doi.org./10.1016/j.jsg.2019.103938.

Ren, Y., Wang, H., and Wen, R. (2017). Imprint of rupture directivity from ground motions of the 24 August 2016 Mw6.2 Central Italy earthquake. *Tectonics, 36,* 3178-3191. https://doi.org/10.1002/2017TC004673.

Ross, Z. E., Trugman, D. T., Azizzadenesheli, K. and Anandkumar, A. (2020). Directivity modes of earthquake populations with unsupervised learning. *J. Geophys. Res. Solid Earth,* 125, e2019JB018299. https://doi.org/10.102972019JB018299.

Ruiz, J. A., Baumont, D., Bernard, P., and Berge-Thierry, C. (2011). Modelling directivity of strong ground motion with a fractal, k^{-2}, kinematic source model. *Geophys. J. Int., 186(1),* 226-244. https://doi.org/10.1111/j.1365-246X.2011.05000.x.

Seekins, L. C., and Boatwright, J. (2010). Rupture directivity of moderate earthquakes in northern California. *Bull. Seism. Soc. Am, 100,* 1107-1119. https://doi:10.1785/0120090161.

723 Sgobba, S., Lanzano, G., and Pacor, F. (2021). Empirical nonergodic shaking scenarios
724 based on spatial correlation models: An application to central Italy. *Earthq. Eng. Struct. D., 50(1),*
725 60-80. https://doi.org/10.1002/eqe.3362.
726 Somerville, P. G., Graves, R. W., and Smith, N. F. (1996). Forward rupture directivity in
727 the Kobe and Northridge earthquakes, and implications for structural engineering. *Seismol. Res.*
728 *Lett., 67*, 55.
729 Somerville, P., Smith, N. F., Graves, W., and Abrahamson, N. (1997). Modification of
730 empirical strong ground motion attenuation relations to include the amplitude and duration effects
731 of rupture directivity. *Seismol. Res. Lett., 68*, 199-222. https://doi.org/10.1785/gssrls.68.1.199.
732 Spagnuolo, E., Herrero, A., and Cultrera, G. (2012). The effect of directivity in a PSHA
733 framework. *Geophys. J. Int., 191*, 616-626. https://doi.org/10.1111/j.1365-246X.2012.05630.x.
734 Spudich, P., and Chiou, B. (2008). Directivity in NGA earthquake ground motions;
735 analysis using isochrone theory. *Earthquake Spectra*, 24, 279-298.
736 https://doi.org/10.1193/1.2928225.
737 Spudich, P., Rowshandel, B., Shahi, S., Baker, J. W., M. EERI. and Chiou, B., S.-J. (2014).
738 Comparison of NGA-West2 Directivity Models, *Earthquake Spectra 30*, 1199-1221.
739 https://doi.org/10.1193/080313EQS222M.
740 Tinti, E., Scognamiglio, L., Michelini, A., and Cocco, M. (2016). Slip heterogeneity and
741 directivity of the ML 6.0. Amatrice earthquake estimated with rapid finite-fault inversion.
742 *Geophys. Res. Lett., 43*, 10745-10752. https://doi.org/10.1002/2016GL071263.
743 Tomic, J., Abercrombie, R. E., and Do Nascimento, A. (2009). Source parameters and
744 rupture velocity of small M ≤ 2.2 reservoir induced earthquakes. *Geophys. J. Int., 179*, 1013-1023.
745 https://doi.org/10.1111/j.1365-246X.2009.04233.x.
746 Trugman, D. T., S. X. Chu, and V. C. Tsai (2021). Earthquake Source Complexity Controls
747 the Frequency Dependence of Near-Source Radiation Patterns. *Geophys. Res. Lett. 48*,
748 e2021GL095022. https://doi.org/10.1002/essoar.10507460.1.
749 Velasco, A. A., Ammon, C. J., and Lay, T. (1994). Empirical Green function deconvolution
750 of broadband surface waves: Rupture directivity of the 1992 Landers, California (Mw = 7.3)
751 earthquake. *Bull. Seism. Soc. Am, 84(3)*, 735-750. https://doi.org/10.1785/BSSA0840030735.
752 Vignaroli, G., Mancini, M., Brilli, M., Bucci, F., Cardinali, M., Giustini, F., Voltaggio, M.,
753 Yu, T. L., and Shen, C. C. (2020). Spatial-temporal evolution of extensional faulting and fluid

754 circulation in the Amatrice Basin (Central Apennines, Italy) during the Pleistocene. *Front. Earth.*
755 *Sci., 8,* 130. https://doi.org/10.3389/feart.2020.00130.
756 Walters, R. J., Elliott, J. R., D'Agostino, N., England, P. C., Hunstad, I., Jackson, J. A.,
757 Parsons, B., Phillips, R. J. and Roberts, G. (2009). The 2009 L'Aquila earthquake (Central Italy):
758 A source mechanism and implications for seismic hazard. *Geophys. Res. Lett., 36,* L17312.
759 https://doi.org/10.1029/2009GL039337.
760 Yamada, T., Mori, J. J., Ide, S., Kawakata, H., Iio, Y., and Ogasawara, H. (2005). Radiation
761 efficiency and apparent stress of small earthquakes in a South African gold mine. *J. Geophys. Res,*
762 *110,* B01305. https://doi.org/10.1029/2004JB003221.
763 Yoshida, K. (2019). Prevalence of asymmetrical rupture in small earthquakes and its effect
764 on the estimation of stress drop: a systematic investigation in inland Japan. *Geosci. Lett. 6,* 16.
765 https://doi.org/10.1186/s40562-019-0145.

766 **a)** **b)**

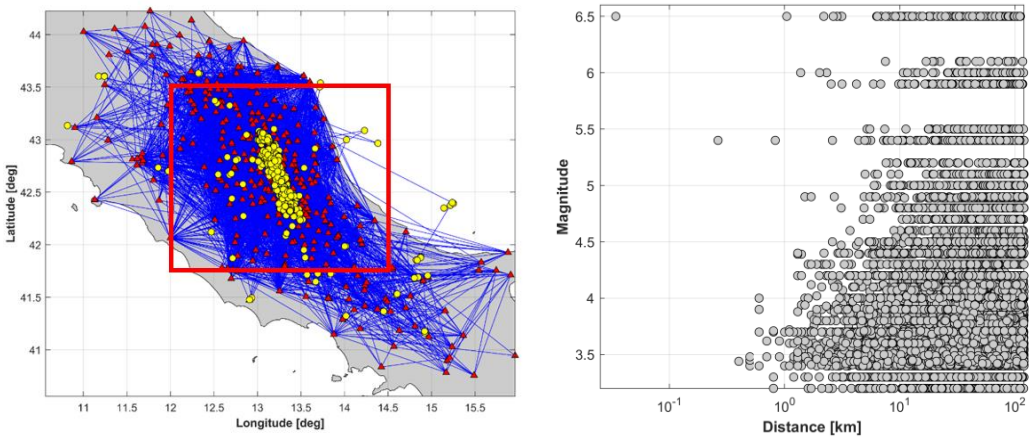

767

768 **Figure 1. a) Map of the coverage by ray-paths (lines) connecting events (yellow circles) and stations (red**
769 **triangles). Red box indicates the study area; b) Plot magnitude-distance from the epicenter. If the Joyner-Boore**
770 **distance is not available, we use the epicentral distance.**

771

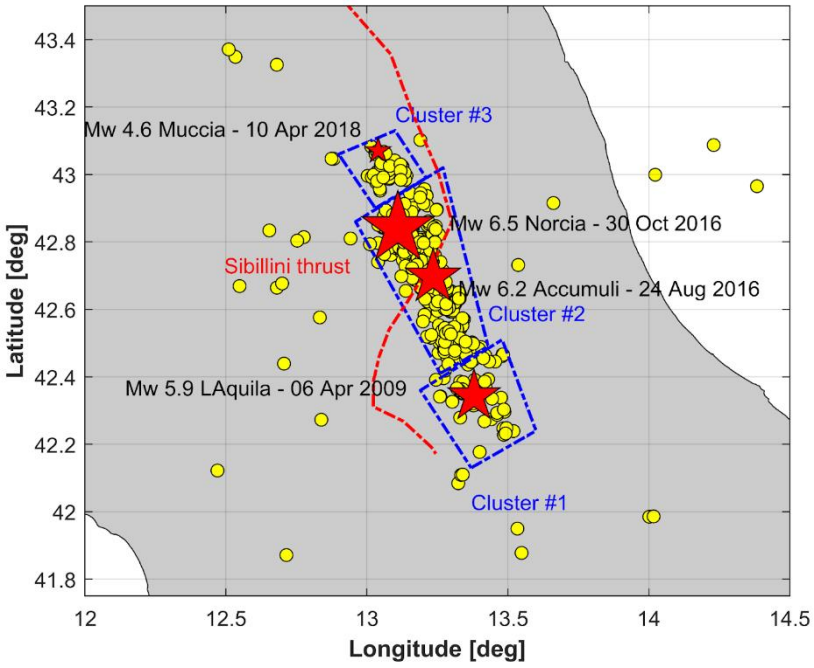

Figure 2. Source areas (with blue dashed boxes) and Mt. Sibillini thrust (with red dashed lines) in a zoomed view with respect to the one shown in Fig. 1a. From South to North: Cluster #1 (main event: L'Aquila 06/04/2009 - 01:32 UTC), #2 (main event: Amatrice 24/08/2016 - 01:36 UTC and Norcia 30/10/2016 06:40 UTC) and #3 (main event: Muccia 10/04/2018 - 03:11 UTC). Red stars represent the mainshocks, while yellow circles are the other events with M > 3.2.

779 **a)** **b)**

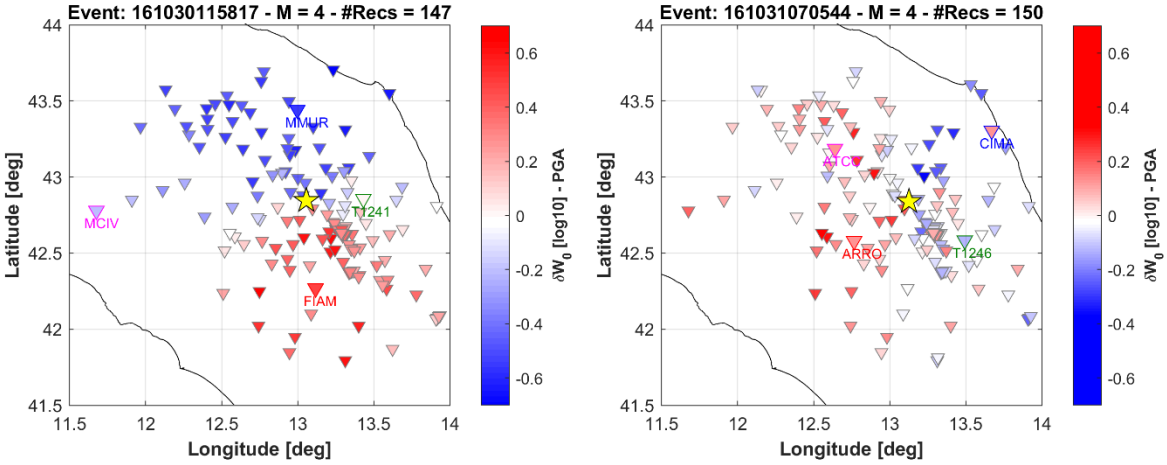

780

781 **c)** **d)**

782

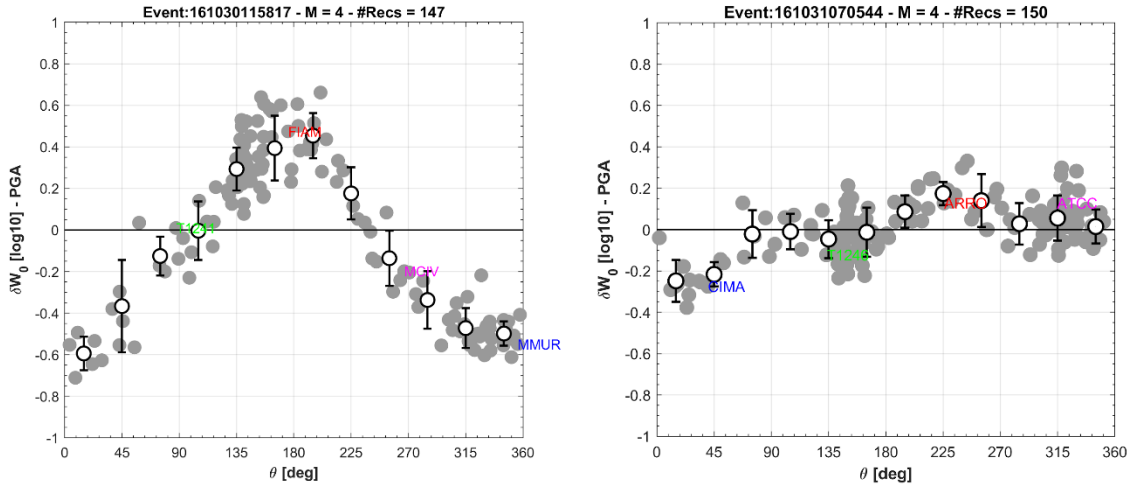

783

784 **Figure 3. Spatial distribution of the PGA residuals δW_0 for the a) M4 event of 30 October 2016 at 11:58:17,**
785 **and b) M4 event of 31 October 2016 at 07:05:44. Yellow stars are the epicenters, while reverse triangles**
786 **represent the stations. Blue/red colors indicate negative/positive residual values (under/over-estimation). The**
787 **labeled stations are used for illustration of the frequency dependence of the residuals in Fig. 4. Locations in the**
788 **four quadrants around the epicenter are highlighted. c)-d) Aleatory residuals δW_0 as a function of θ for the**
789 **same events in a) and b), respectively.**

790

791

792 **a)** **b)**

793

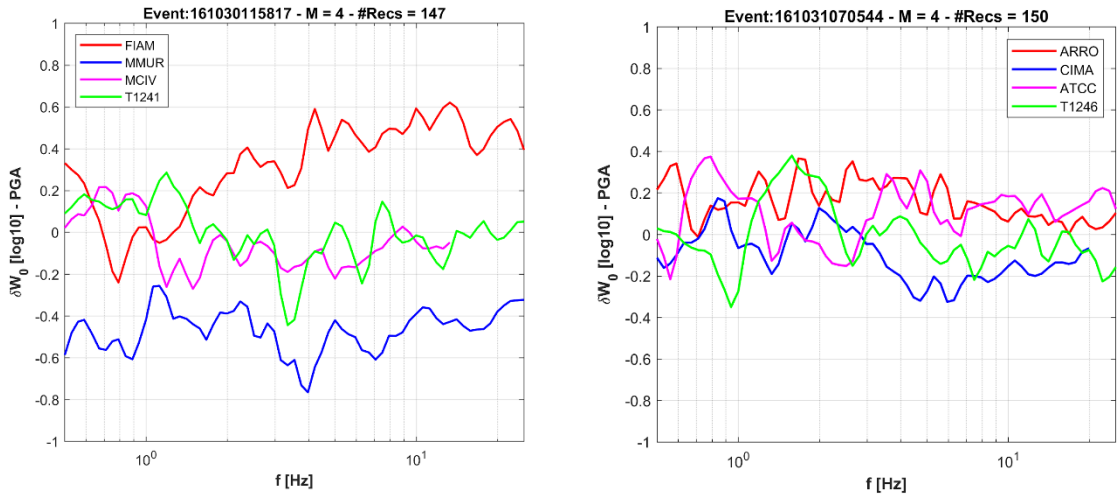

794

795 **Figure 4. Trend of δW_0 vs frequency for the 4 stations shown in Figure 3, for a) the M4 event of 30 October**
796 **2016 at 11:58:17, and b) the M4 event of 31 October 2016 at 07:05:44.**

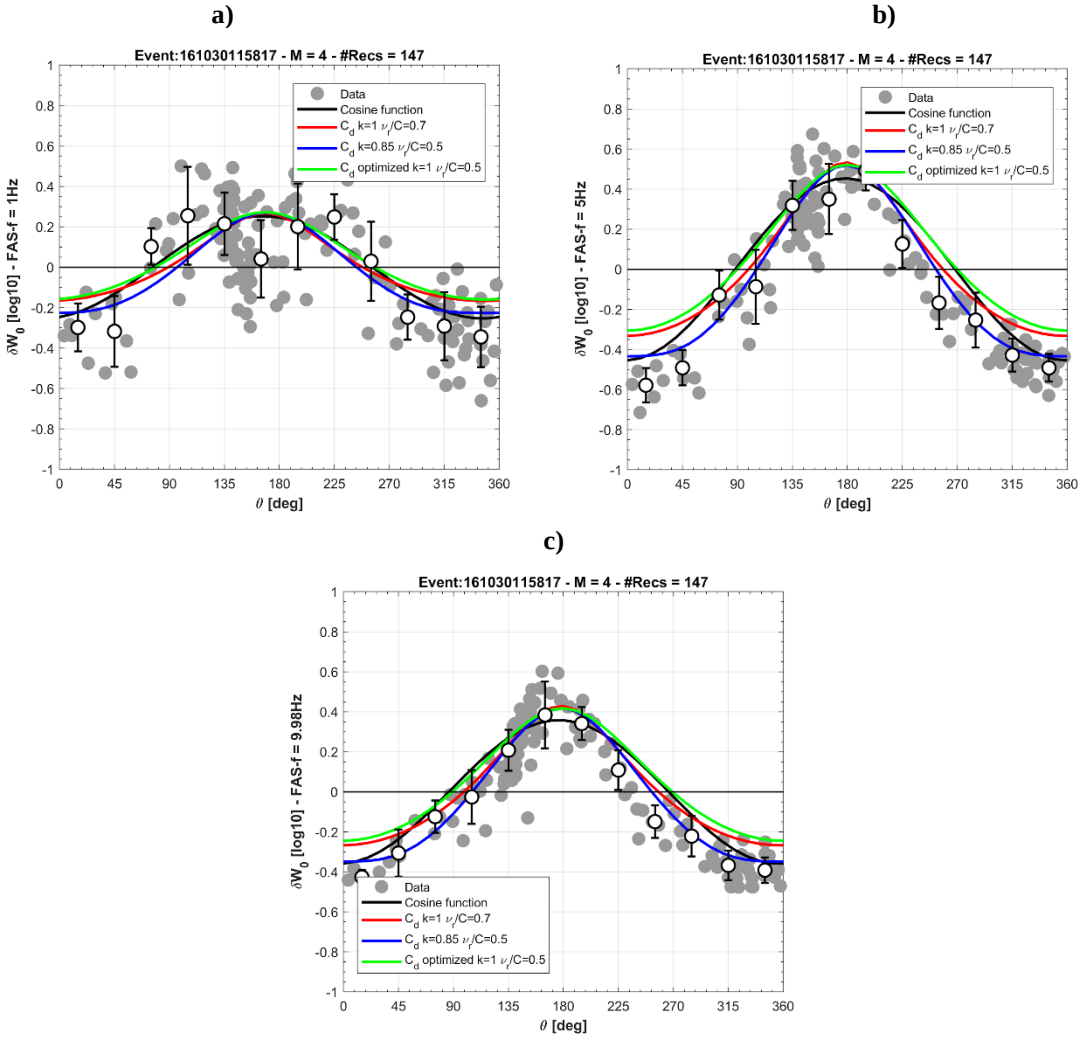

Figure 5. Azimuthal variation of the aleatory residuals for a Mw 4.0 event of 30 October 2016, 11:58:17 at a) f=1 Hz, c) f=5 Hz, e) f=10 Hz. In black, fit with cosinusoidal function (Case I), in red fit with k = 1 and α= 0.7 (Case II), in blue α = 0.5 and k = 0.85 (Case III), while with the green curve the fit is estimated with an optimization algorithm (in this case, k tends to 1 and α is close to 0.5 - Case IV).

a) **b)**

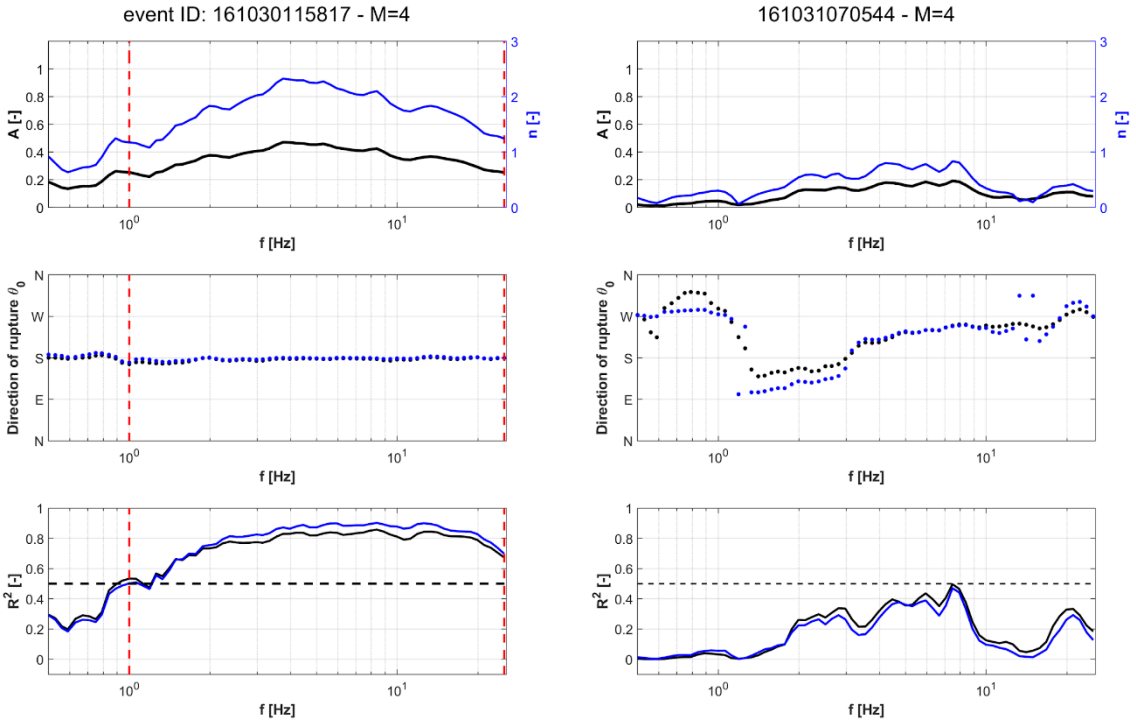

Figure 6. Directivity amplitude (top); direction of rupture propagation (middle); coefficient of determination (bottom) plotted versus frequency. The black curve represents the fitting results with the cosine model, the blue curve with the C_d model. Red lines represent the minimum and maximum frequency within which the *proxy* R^2 is larger than 0.5. a) M4 event of 30 October 2016 at 11:58:17; b) M4 event of 31 October 2016 at 07:05:44.

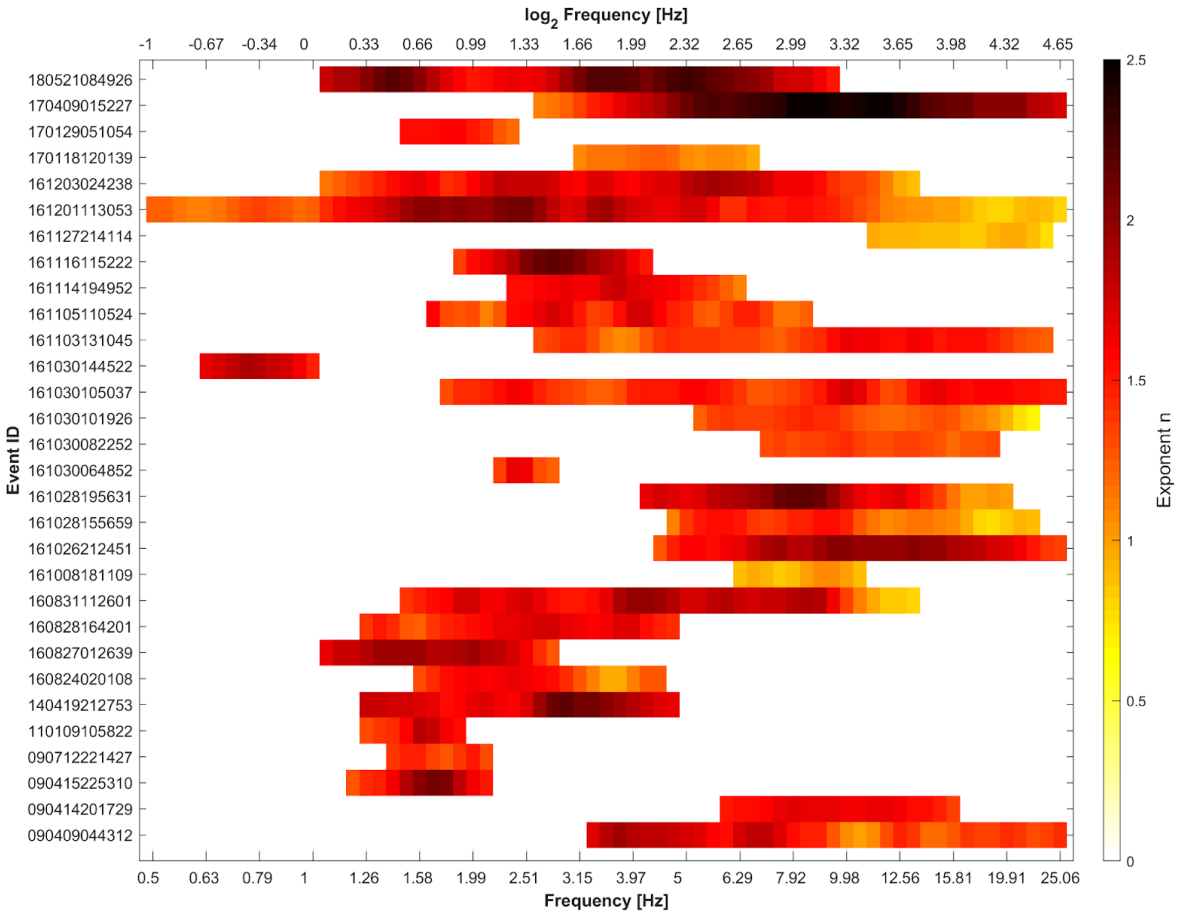

Figure 7. Directivity frequency bandwidth of the events in the magnitude range from 3.7 to 4.0. Each frequency interval of the bandwidth (on x-axis) is colored according to the value of amplitude n. Since the frequency range is logarithmically equispaced, at the top part of x-axis is shown the log2 frequency, and the corresponding frequency content is shown at the bottom part of x-axis.

817

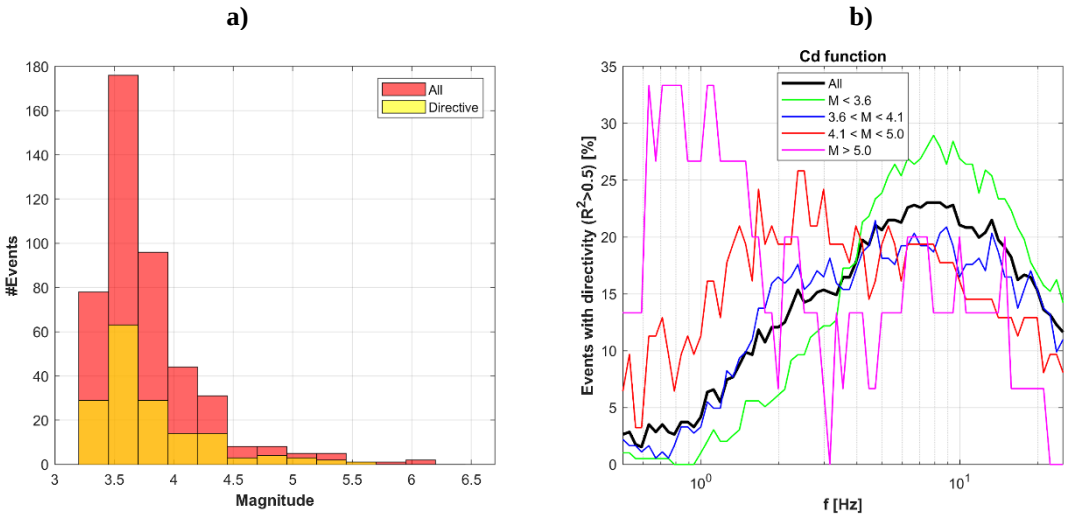

818

819 **Figure 8. a) Number of directive events (yellow) compared to the event distributions (red) of the study dataset,**
820 **grouped in magnitude bins. b) Percentage of the events with R^2 > 0.5 out of the total number of events as a**
821 **function of frequency for different magnitude intervals (see legend).**

822

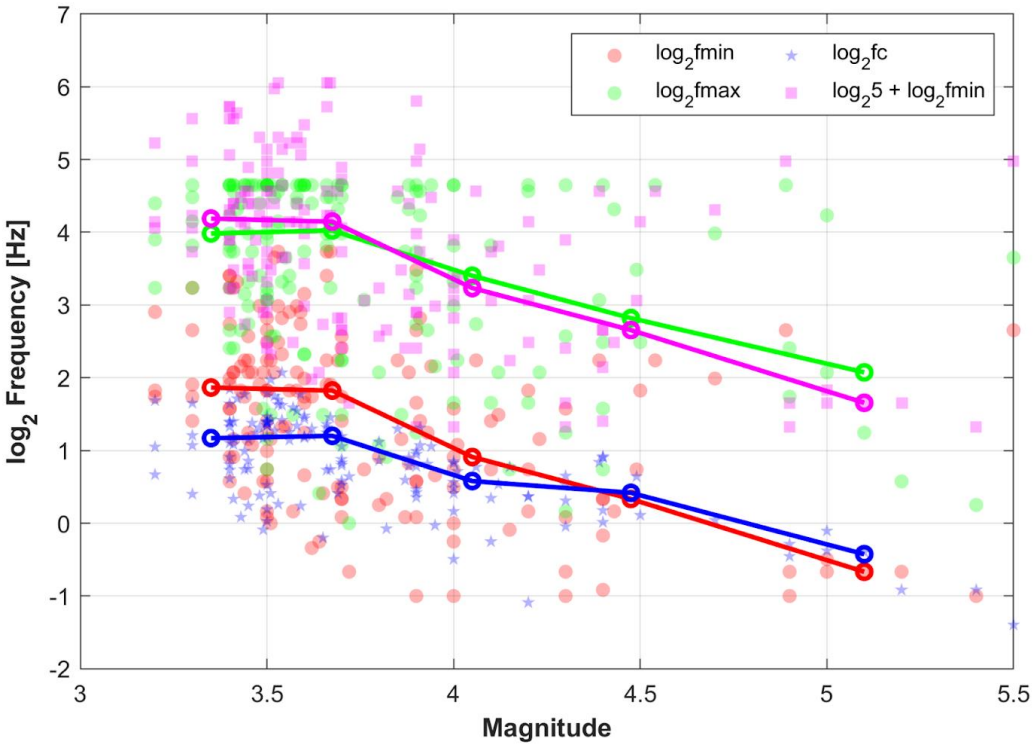

Figure 9. Minimum frequency (log2 f_{min}, red dots) and maximum frequency (log2 f_{max}, green dots) where the directivity effect is present plotted as a function of magnitude. Blue stars are the corner frequency from Bindi et al. (2018) and magenta squares are the values obtained by multiplying the minimum frequency by a factor of 5. Solid lines represent the median values over magnitude bin width.

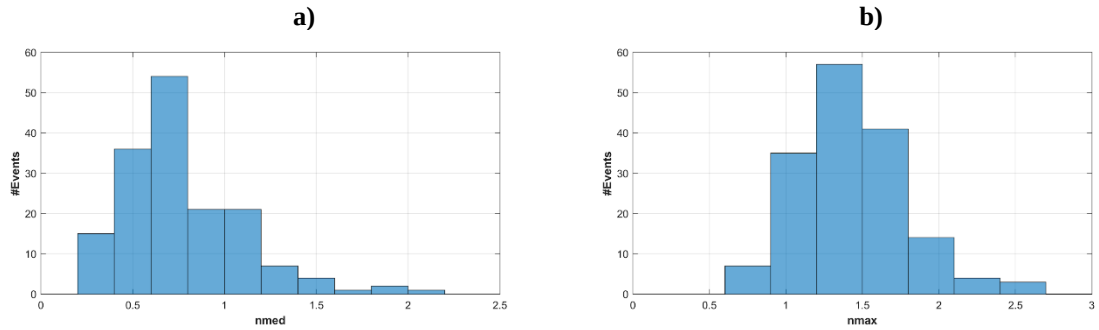

Figure 10. a) Median and b) maximum value of the exponent *n* for the events with directivity among all observed frequency ranges.

835

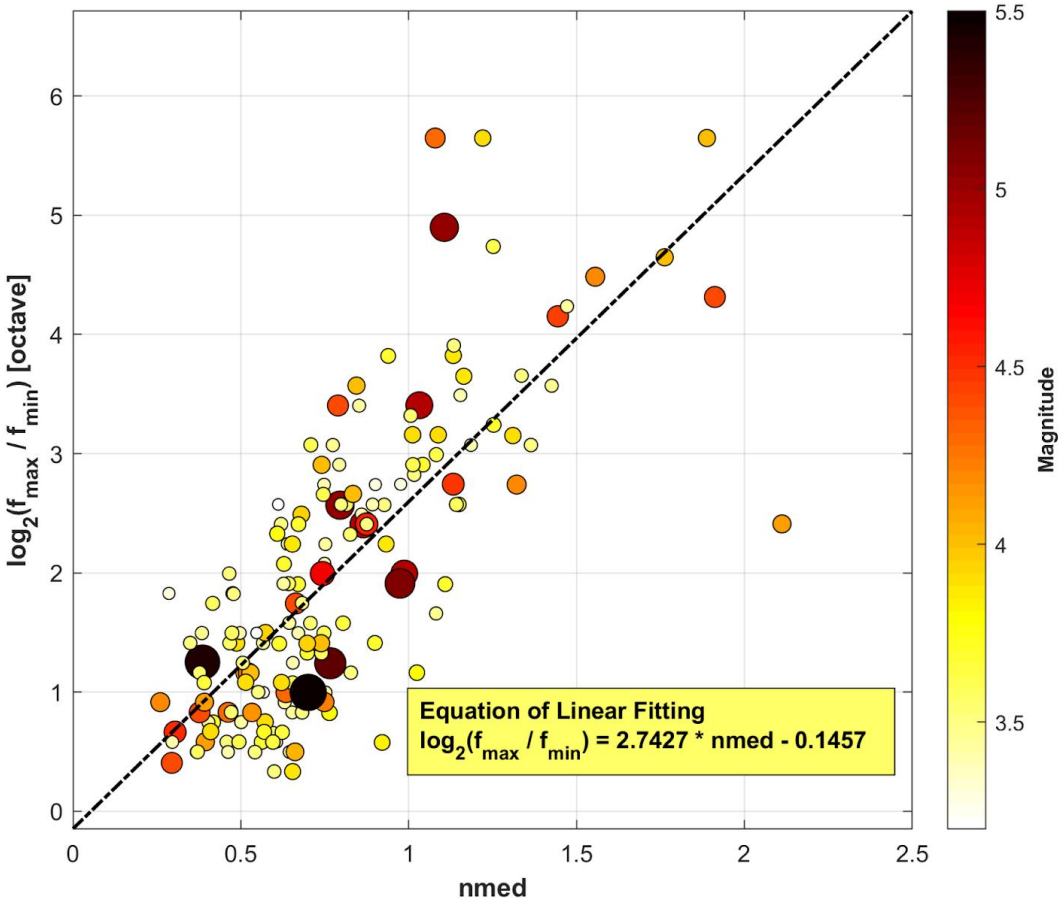

836

837 **Figure 11. Frequency bandwidth against values n_{med}. The size of the circles is proportional to the magnitude;**
838 **black dashed line represents the fit curve. The yellow box shows the empirical linear relation between the**
839 **frequency bandwidth and n_{med}.**

840

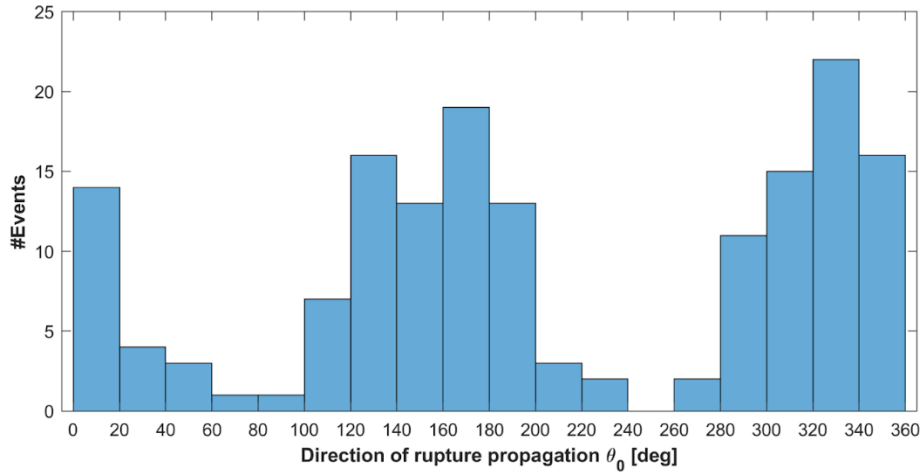

841
842 **Figure 12. Median value of the direction of rupture propagation for all the directive events.**

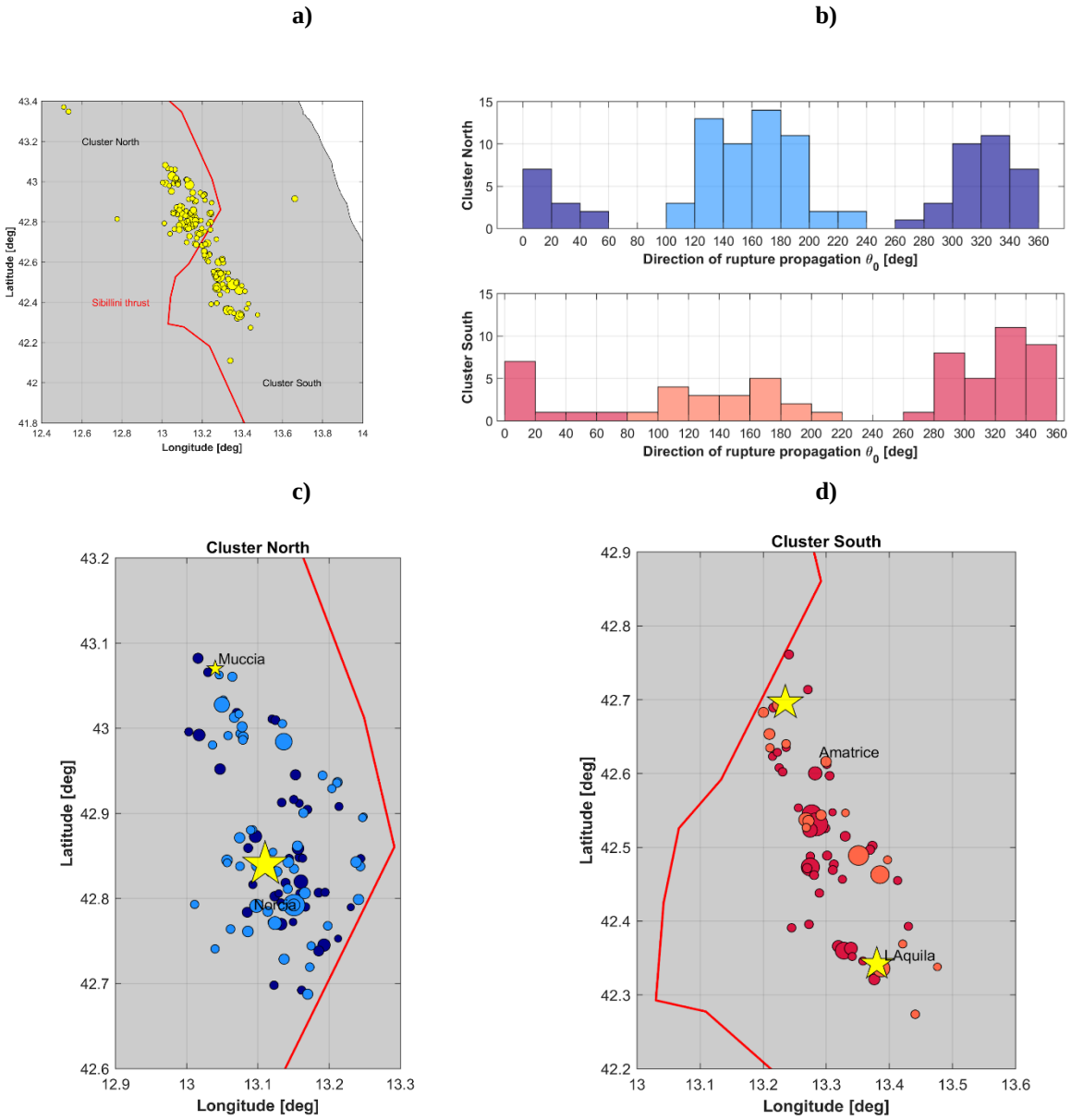

Figure 13. a) Map of the events (yellow dots, size is proportional to the magnitude) divided in a cluster at the North and at the South with respect to the Mt. Sibillini thrust (red line). b) Distribution of the median values of the direction of rupture propagation for the two clusters: bluish colors for the northern cluster, reddish colors for the southern cluster. c) Events with directivity in the cluster North and d) in the cluster South. For the cluster North, events with direction of rupture propagation towards North (270-90°) are in light blue while the ones with direction towards South (270-90°) are in dark blue. For the cluster South, events towards North are in light red and towards South in dark red. Yellow stars are the mainshocks for the analyzed earthquakes.

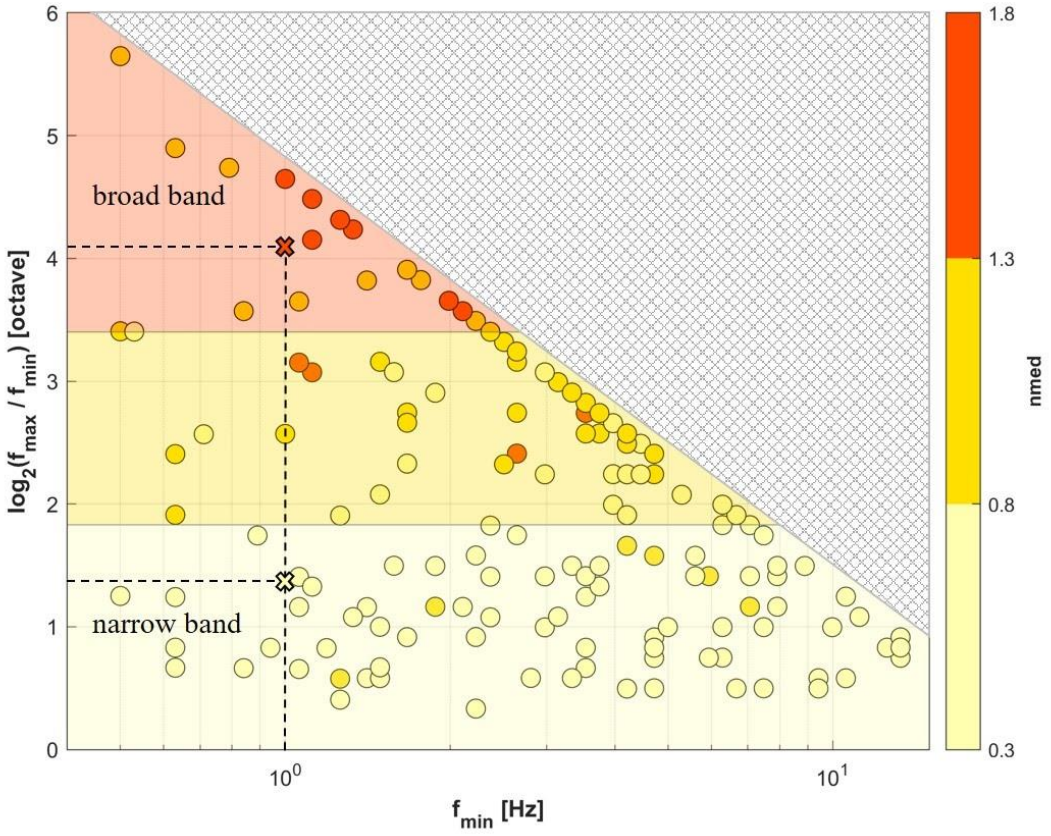

Fig. 14 Relation between minimum frequency f_{min} and bandwidth, defined as $\log 2 \frac{f_{max}}{f_{min}}$. The color of the circles represent the value of n_{med}. Three domains are shown in the graph, defined according to the 75th percentile. With crosses, it shows how we can classify an event with Mw 4.6, where $f_{min} = f_c$, equal at about 1 Hz (see Fig. 11). Light-yellow cross shows an event with weak directivity (input value $n_{med} = 0.55$) where $\log 2 \frac{f_{max}}{f_{min}}$ is equal to 1.36 octaves; red cross represent the case with high directivity (input value $n_{med} = 1.55$) and $\log 2 \frac{f_{max}}{f_{min}}$ equal to 4.1 octaves. The large grey triangle with mesh net in the upper right portion of the graph defines the limit of the existence domain of our frequency interval, where $f_{max} = 25$ Hz.

a)

Case	A or n	θ_0(°)	R^2	σ
I	0.2534	166.34	0.5338	0.1884
II	0.5770	168.52	0.4436	0.2050
III	1.1736	169.74	0.5024	0.1988
IV	0.9062	168.41	0.5186	0.1996

b)

Case	A or n	θ_0(°)	R^2	σ
I	0.4537	178.17	0.8200	0.1410
II	1.1488	178.66	0.8011	0.1415
III	2.2469	179.06	0.8732	0.1289
IV	1.7347	179.87	0.8108	0.1452

c)

Case	A or n	θ_0(°)	R^2	σ
I	0.3586	176.26	0.8118	0.1169
II	0.9248	178.19	0.8123	0.1079
III	1.8064	178.87	0.8786	0.1007
IV	1.3872	179.17	0.8200	0.1154

Table 1. Values of amplitude (A or n), azimuth θ_0, coefficient of determination R^2 and standard deviation σ for different cases reported in Fig. 5. a) f=1 Hz, b) f=5 Hz, c) f=10 Hz.